A Study of the Position-Dependent Response of Thermal Kinetic Inductance Detectors Through the Use of Cryogenic Beam Steering

Ian Fogarty Florang, Jonathan William Dean, Joseph W. Fowler, Tom-Erik Haugen, Shannon F. Hoogerheide, Daniel Jardin, H. Pieter Mumm, Nathan Nakamura, Matthew R. Natale, Galen C. O'Neil, Nathan J. Ortiz, Jeremy Paster, Thomas M. Rao, Avirup Roy, Daniel S. Swetz, Joel N. Ullom, Michael R. Vissers, and Paul Szypryt

***Abstract*—There are a number of considerations when designing a low-temperature detector for the best possible energy resolution. One that has been particularly challenging for thermal kinetic inductance detectors (TKIDs) is ensuring that the detector's response to deposited energy is constant across the active area of a single pixel. In this article, we directly probe the position-dependent response of our TKID devices at 100-μm-scale resolution through the use of a pulsed laser beam steered with a cryogenic microelectromechanical system mirror. We observe position-dependent response that could limit the energy resolution of our current devices to the part per ten scale. We find that the position-dependent response is strongly correlated with the local current density in the TKID inductor, although the thermal physics and geometry associated with the micromachined absorber also likely have a nonnegligible effect. Finally, we suggest analysis methods and design considerations that could reduce the severity of this position dependence, and we argue that there is significant potential for further improvement.**

***Index Terms*—Low-temperature detectors, quantum calorimeters, thermal kinetic inductance detectors (TKIDs).**

Received 26 September 2025; revised 25 February 2026; accepted 22 March 2026. Date of publication 2 April 2026; date of current version 16 April 2026. This work was supported in part by the U.S. Department of Energy (DOE) Office of Science, Office of Nuclear Physics, under Grant DE-SC0021415 and Grant DE-SC0023682, and in part by the U.S. Department of Commerce, National Institute of Standards and Technology under Grant 70NANB23H027. *(Corresponding author: Ian Fogarty Florang.)*

Ian Fogarty Florang, Jonathan William Dean, Matthew R. Natale, Avirup Roy, and Paul Szypryt are with the Department of Physics, University of Colorado, Boulder CO 80309 USA, and also with the Quantum Sensors Division, National Institute of Standards and Technology, Boulder CO 80305 USA (e-mail: ian.fogartyflorang@colorado.edu; jonathan.dean@nist.gov; matthew.natale@nist.gov; avirup.roy@nist.gov; paul.szypryt@nist.gov).

Joseph W. Fowler, Nathan Nakamura, Galen C. O'Neil, Nathan J. Ortiz, Daniel S. Swetz, Joel N. Ullom, and Michael R. Vissers are with the Quantum Sensors Division, National Institute of Standards and Technology, Boulder CO 80305 USA (e-mail: joe.fowler@nist.gov; nathan.nakamura@nist.gov; galen.oneil@nist.gov; nathan.ortiz@nist.gov; daniel.swetz@nist.gov; joel.ullom@nist.gov; michael.vissers@nist.gov).

Tom-Erik Haugen, Shannon F. Hoogerheide, Daniel Jardin, H. Pieter Mumm, Jeremy Paster, and Thomas M. Rao are with the Radiation Physics Division, National Institute of Standards and Technology, Gaithersburg, MD 20899 USA (e-mail: tom-erik.haugen@nist.gov; shannon.hoogerheide@nist.gov; daniel.jardin@nist.gov; hans.mumm@nist.gov; jeremy.paster@nist.gov; thomas.rao@nist.gov).

Color versions of one or more figures in this article are available at https://doi.org/10.1109/TASC.2026.3680384.

Digital Object Identifier 10.1109/TASC.2026.3680384

I. Introduction

Microcalorimeters based on the superconducting transition-edge sensor (TES) [1], [2], [3] are increasingly being used in a growing number of precision spectroscopy applications, such as beamline physics [4], [5], exotic atom spectroscopy [6], [7], [8], spectral line metrology [9], [10], and X-ray/gamma-ray astronomy [11], [12]. These devices are typically read out using superconducting quantum interference devices (SQUIDs) [13], [14], and various SQUID-based multiplexing techniques have been developed to read out arrays containing hundreds of TES calorimeters [15], [16], [17], [18]. The TES calorimeter is now a relatively mature low-temperature detector technology, but scaling the SQUID readout systems for very large arrays of thousands of devices becomes progressively more challenging due to fabrication complexity, physical footprint of cryogenic circuits, and room-temperature microwave electronics costs, among other issues.

Here, we instead consider a variant of the kinetic inductance detector (KID) [19], [20], [21] optimized for thermal calorimeter operation. This thermal kinetic inductance detector (TKID) [22], [23], [24], [25] makes use of a dedicated absorber to stop highly energetic photons and charged particles, converting the deposited energy into a rise in absorber temperature that changes the kinetic inductance of the TKID superconductor. This change in inductance is sensed by measuring its effect on the frequency of the resonant circuit embedded in the TKID. In this way, TKIDs combine the thermal detection properties of cryogenic calorimeters with the ease of multiplexing of KIDs, providing a straightforward path for large detector arrays. Arrays of KIDs optimized for visible to near-infrared detection have reached pixel counts in the 10-kilopixel range [26]. In addition, unlike a TES calorimeter, which can have dynamic range limited by the narrow superconducting-to-normal transition region, TKIDs have shown excellent linearity across a wide range of energies [27], and this dynamic range can potentially be improved with advanced readout techniques, such as tone-tracking. We have recently utilized prototype TKIDs to spectroscopically characterize the ionizing radiation background in an environment representative of superconducting qubit devices [27], [28]. We are also developing large-active-area TKID arrays for measurements of free neutron beta decay and other fundamental symmetry studies [29], [30].

The TKIDs developed thus far have unfortunately shown worse energy resolution than their TES calorimeter counterparts, despite the fact that similar resolutions are expected from thermal noise model estimates [24], [31]. This energy resolution degradation is an active area of study, but position dependence in the TKID response function has long been thought to be a contributing factor [23], [32], [33]. For example, the TKID may have a larger response (resonant frequency shift) for events that deposit their energy at the center of the absorber as opposed to near one of the sidewalls.

In this article, we experimentally characterize this position-dependent response through the use of a focused laser spot that can be steered across a single TKID pixel. Steering is achieved with a cryogenic microelectromechanical system (MEMS) mirror attached to the same cryogenic stage as the TKID. We compare the measured TKID response to simulated current densities in the TKID inductor and show that areas of higher current density have elevated pulse response. We also see evidence for additional position dependence that is not related to the local current density of the superconductor and rather is likely due to the thermal properties and geometry of the micromachined absorber.

II. Experimental Setup

A. TKID Description

Here, we summarize the most relevant parameters of the TKID device used in this study, and a more detailed description can be found in [27]. The TKID resonator is formed from a 200-nm-thick substoichiometric TiN thin film sputtered on a 1.5-mm-thick Si substrate (see Fig. 1). This substoichiometric TiN film consists of alternating layers of stoichiometric TiN and Ti, done to control the superconducting critical temperature (T_c) of the film, here ~850 mK, through the proximity effect [34], [35].

The TKID microresonator has a resonant frequency of 1.283 GHz and intrinsic quality factor $Q_i \approx 3.4 \times 10^4$ at the operating temperature of 175 mK. The device is capacitively coupled to a microstrip transmission line (also TiN) with a coupling quality factor $Q_c \approx 4.2 \times 10^3$. The total quality factor, Q, is therefore largely coupling limited, and the bandwidth of the resonator is ~340 kHz. The device was cooled using a commercial adiabatic demagnetization refrigerator backed by an He-3 sorption cooler. A standard vector network analyzer was used to measure the complex transmission across the device, and these resonator properties were extracted from a Lorentzian fit to the complex transmission magnitude.

The absorbing island is lithographically defined with a deep reactive ion etch (DRIE) through the full Si wafer thickness (1.5 mm). The island has an area of roughly 5.0 mm × 4.6 mm, resulting in an Si absorber volume of 34.5 mm^3 and heat capacity $C \approx 7.6 \times 10^8$ eV/K at 175 mK. The absorber is supported by a set of four legs connected to the bulk Si substrate, which provides a weak thermal link to the heat bath. The legs are 2.0 mm long and 0.2 mm wide, resulting in a total thermal conductivity $G \approx 8.4 \times 10^{12}$ eV/s/K. This gives the TKID an expected thermal decay time of 91 μs. Turns in the leg geometry are used to mitigate ballistic phonon escape. To efficiently remove heat from the bulk frame of the device, Au pads are deposited along the chip perimeter, and Au wire bonds connect these pads to the Cu device box rigidly mounted to the cryostat cold stage. The faces of the Cu device box near the TKID chip are blackened with permanent marker to limit reflection of stray light.

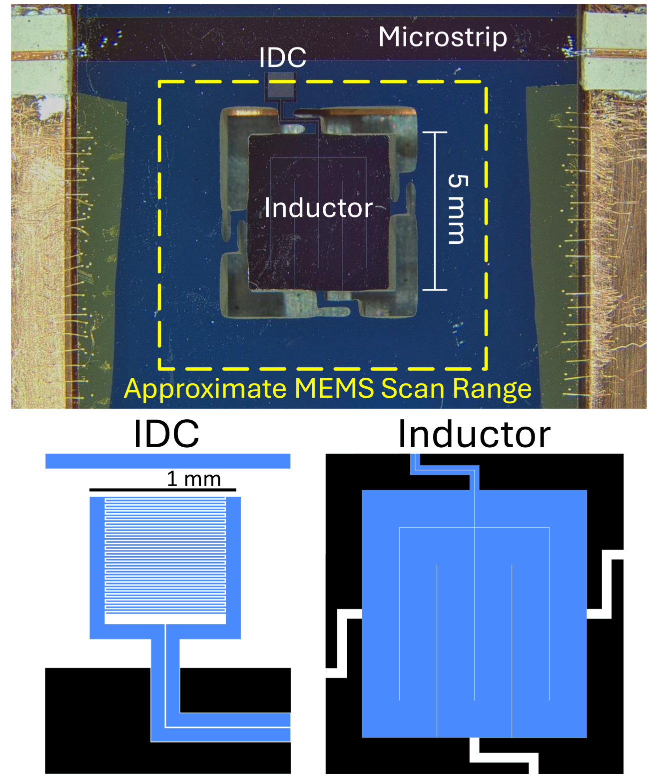

Fig. 1. TKID micrograph and schematic. The upper panel shows a micrograph of the TKID used in this paper, while the lower panels show schematics of the IDC and meandered inductor with TiN shown in light blue, Si shown in white, and removed material shown in black. The superconducting resonator consists of a 200-nm-thick TiN film that is patterned into a meandered inductor, IDC, and microstrip feedline. The TKID is capacitively coupled to the microstrip feedline to read out the TKID pulse response. The inductor consists of a 700-μm-wide meander with 10 μm gaps and sits atop a 1.5-mm-thick, lithographically defined island of Si that acts as the TKID's absorber. The absorber is thermally coupled by four legs to the bulk Si (the "frame") of the chip, which in turn is thermally sunk to the Cu device box via Au bond pads and wirebonds. The deep etch that defines the island and legs was imperfect, resulting in some variation in the geometry of these features. The yellow dashed box in the micrograph approximates the MEMS mirror's scan range.

B. Cryogenic Beam Steering With MEMS Mirror

For these measurements, a MEMS mirror was used to direct photon pulses at various points across the back (side without the superconducting film) of our TKID, as shown in Fig. 2. Building upon previous work demonstrating MEMS mirror-based laser scanning [36], our optical setup is similar to that described in [37], but some changes were made to adapt it to our experimental setup. First, we use a 635-nm laser diode coupled into a single-mode fiber with a core diameter of 8.2 μm and a numerical aperture of 0.14. We note that this optical fiber has

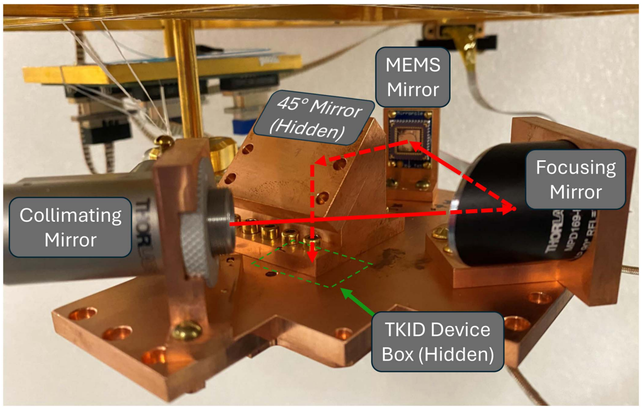

Fig. 2. Cold stage optical assembly. Optical components match those described in [37] except for the optical fiber and coupled laser diode, which are described in the text. The red lines in the figure show the laser's path, with dashed lines representing portions of the path that are obscured in the image. The laser fiber is coupled into the collimating mirror and then directed to the focusing mirror. The focused beam is then reflected off the MEMS mirror and onto the 45° mirror, which sends the beam onto the back side of the TKID. The MEMS mirror can vary its angle to point the beam at different locations across the TKID chip.

been optimized for use at longer wavelengths, potentially resulting in some distortion of the otherwise Gaussian beam profile leaving the fiber. Second, due to mechanical constraints, the TKID is positioned approximately 800 μm away from the focal point of the off-axis parabolic focusing mirror. Together, these changes result in a theoretical beam full-width at half-maximum (FWHM) [37] of roughly 30 μm at the TKID. In addition, there is some flexibility in positioning the polytetrafluoroethylene fiber ferrule termination at the collimator input of the optical assembly, resulting in some additional uncertainty in the beam spot size estimation.

The spot size was experimentally verified at cryogenic temperatures by scanning the laser beam across the edge of the TKID device where the response drops significantly. The measured beam intensity was fit to a Gaussian distribution, resulting in a beam FWHM of 100 ± 5 μm. We expect the positioning of the ferrule within the collimator to be the main source of discrepancy between the theoretical and measured spot sizes.

C. Data Collection and Processing

Data for this study were collected with the device temperature controlled at 175 mK, which we previously found to provide maximum signal to noise in the pulse response [27]. Energy deposition events were measured using a microwave homodyne readout system, typical in KID measurements and described in detail in other works [20], [38]. For all measurements, the readout tone was fixed at the resonant frequency of the TKID and the tone power was set to a few dB below the onset of bifurcation. This homodyne setup was used to sample the complex transmission at a rate of 1.25 MHz.

Typically, the phase response of a KID device is stronger than its dissipation counterpart [20]. For this reason, it is often useful to extract the phase response from the complex transmission data and analyze only the phase time series. Here, this is accomplished by first sweeping the complex transmission of the TKID device in the absence of illumination at frequencies near its resonance, resulting in a roughly circular pattern in the complex plane. In subsequent photon absorption events, we quantify the device's phase response by the angle subtended by the arc of points moving along this circle. We will refer to this angle as the "phase shift" of the resonator, but to be clear: we are not tone tracking the resonance during pulses.

To measure the position dependence of the TKID, a function generator was used to drive the 635-nm laser diode with a pulse width of 1 μs and a repetition rate of 250 Hz, providing sufficient time for the TKID to recover after each pulse. Based on calibrated measurements made previously with this TKID [27], we estimate the energy deposited in the TKID chip by each laser pulse was on the order of 1 MeV. While the laser was pulsed, the MEMS mirror repeatedly traced out a raster pattern across the TKID with continuous spatial resolution in the x-direction but discrete resolution in the y-direction due to the finite number of lines (100) included in the raster scan. The I and Q data were recorded for a total of one hour, resulting in 32 raster scan iterations.

Due to the preliminary nature of our experimental setup, we were unable to synchronize the movement of the MEMS mirror with the timing of our laser pulses in hardware. We instead used Fourier analysis techniques, specifically phase dispersion minimization [39], to back out relevant times from our data in postprocessing, including the MEMS mirror line time and full raster period. Using these extracted timescales, we converted the arrival time of each laser pulse to a position in the x–y plane, which we then mapped to physical locations based on the nominal TKID geometry. Pulses were then grouped into bins based on their position, and the peak heights of pulses within each bin were averaged together to estimate the local TKID responsivity.

III. Results and Analysis

Fig. 3 shows the response of our TKID as a function of laser position, with the upper panel showing the entire 2-D distribution and the lower panel showing four horizontal slices at different y positions to show more clearly the quantitative variation of the device response across the chip. The color in the upper panel represents the average peak phase shift of pulses in each region. The TKID island and the four legs connecting it to the Si frame are visible in the center of the upper panel, and the frame itself is clearly distinguished from the region between the island and frame where minimal light is absorbed in the Si. The region of the TKID above $y = 3.5$ mm is blocked by the Cu device box, so minimal response is expected there.

We identify the following five major features in the position dependence of the TKID's response.

1) There are several band-shaped regions within the island where the response is enhanced compared to adjacent regions. There is an M-shaped region where device response is about 10% higher than adjacent areas, and there are two fainter vertical bands between the legs of the M where response is also slightly enhanced, on the order of 3%.

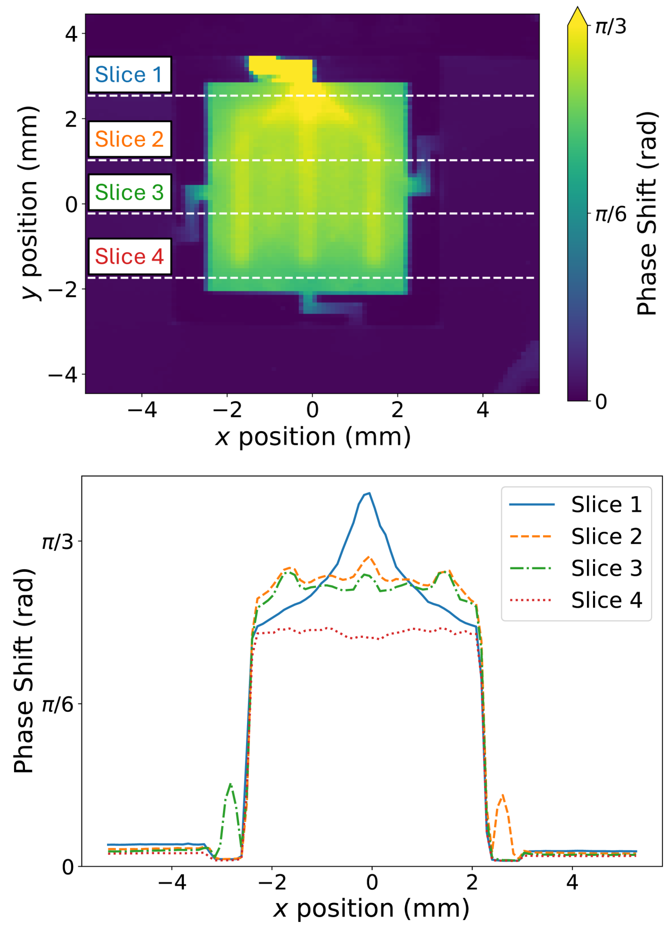

Fig. 3. TKID pulse responsivity as a function of position. The upper panel shows pulse peak phase shift as a function of x and y positions, while the lower panel shows four horizontal slices from the complete dataset. The locations of these slices are indicated in the upper panel by white dashed lines, each labeled with their corresponding number and trace color. Slices 2 and 3 show banding behavior in the device response, with three large peaks and two smaller ones between them. They also show the left and right legs of the TKID, which appear as additional peaks on the sides of the main response region. Slices 1 and 4 show that device response drops near the edges of the island, although slice 1 also shows a significant increase in response near the upper leg, which carries the TiN trace that connects the IDC and inductor. Note that in the upper panel there are pulses that have a peak phase shift greater than $\pi/3$ rad, but the color scale is limited to emphasize the features on the island.

2) There is a triangular region near the top of the TKID where response is further increased.
3) Response drops by about 20% between the center of the island and the edge, and this drop is more significant near all legs except the upper one.
4) In contrast to the three other legs, the upper leg shows the strongest response in the TKID, with an average pulse height about 2.5 times larger than the average pulse height of the TKID island.
5) The device shows nonzero response to events that happen on the Si frame, with pulse heights about 5% of those on the island.

Each of these features contributes to variation in pulse height of on order a part in ten, potentially limiting the energy resolution of this or a similar device to the same level. An understanding

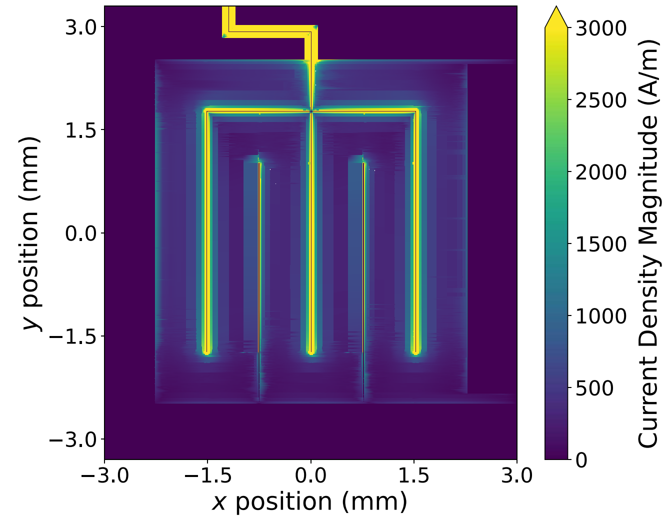

Fig. 4. Simulation of current flow in TKID TiN film. The data in this plot come from a Sonnet simulation of the TKID. The microstrip feedline and IDC are omitted because they are blocked from the MEMS mirror by the Cu device box. The currents crowd around the gaps in the meandered inductor, particularly those that connect to the leads on the upper leg. The current distribution closely matches the banding in the TKID pulse response seen in Fig. 3.

of each of these effects will likely be important to explain TKID energy resolution, but this article will focus on features one and four: the banding and the increased response in the upper leg. Future work will be done to examine the other features in depth.

Previous simulation work has suggested that current density distribution could be a source of position-dependent response in KIDs due to kinetic inductance nonlinearities [33], so this was one of the first effects that we examined. To do so, we modeled the currents in our TKID using the numerical electromagnetic simulation software Sonnet, and the results are shown in Fig. 4, where color indicates the magnitude of the local current density in the superconducting film. One can see that the current is expected to crowd around the gaps in the inductor trace, with the strongest currents near the gaps that connect to the upper leg. This closely matches the M-shaped region of high responsivity shown in Fig. 3. Similarly, the gaps that protrude from the bottom edge of the inductor align with the fainter bands that appear in Fig. 3 and show correspondingly less current crowding. The leads along the upper leg likewise show high current density, largely expected behavior given the TiN is much narrower in this region.

Given that the TKID is backside illuminated and the attenuation length of 635 nm light in Si is significantly shorter than the thickness of the TKID absorber, none of the laser photons should interact directly with the TiN film. However, the correlation between the current density and device response suggests there is some localized behavior in the device before it thermalizes. Such behavior likely varies on a timescale different from the device's thermal behavior, so to examine this, we fit each averaged pulse with a two-decay-time pulse shape of the functional form

$$s(t) = A_{\mathrm{f}}\left[e^{-(t-t_0)/\tau_{\mathrm{f}}} - e^{-(t-t_0)/\tau_{\mathrm{r}}}\right] + A_{\mathrm{s}}\left[e^{-(t-t_0)/\tau_{\mathrm{s}}} - e^{-(t-t_0)/\tau_{\mathrm{r}}}\right] \quad (1)$$

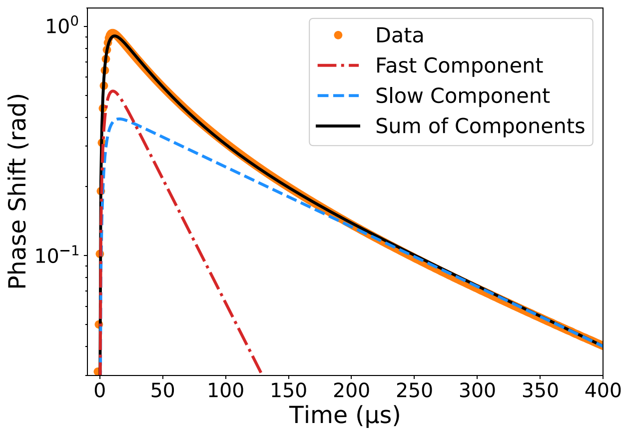

Fig. 5. Two-decay-time pulse fit example. An averaged pulse (orange dots) is compared to a two-decay-time pulse fit (solid black line) of the functional form given in (1). The fast (red dot-dash line) and slow (blue dashed line) components of the fit are also plotted separately to show where they each dominate the pulse shape.

where $s(t)$ is the pulse height as a function of time, t_0 is the pulse start time, τ_r is the pulse rise time, and subscripts f and s refer to the fast and slow components of the pulse decay, respectively, with corresponding amplitudes A and decay times τ. Fig. 5 shows the result of fitting (1) to an arbitrary averaged pulse from our position-dependent study, with the fast and slow components plotted individually to show where each component dominates the fitted pulse shape.

When allowing all six parameters to vary and fitting average pulses from a few different regions of the TKID island, we find that most parameters vary by less than 2%; the only two parameters that vary by more are the amplitudes A_f and A_s. Our fits give a rise time of 4 μs, a fast-decay time of 41 μs, and a slow-decay time of 168 μs. The rise time is comparable to the expected resonator response time of $\sim$3 μs, given by the inverse of the resonator bandwidth, and the fast-decay time is compatible with previous measurements of the quasiparticle recombination time in TiN films [35]. We then interpret the slow-decay time as the thermal decay time of the TKID island. While the fitted value is roughly twice the theoretical value given in Section II-A, we believe this is reasonable given several points: first, we have seen in previous devices that sharp corners in membrane legs decrease thermal conductance, and second, the heat capacity of the TKID is potentially larger than designed due to fabrication defects and byproducts. Together, these effects would slow the detector's thermal relaxation.

Given that only the amplitudes showed significant variation, we repeated our fitting with all nonamplitude parameters fixed, this time for every averaged pulse that comprises the responsivity map in Fig. 3. The distributions of A_f and A_s as functions of position are shown in Fig. 6. One can see a stark contrast: while the fast component matches the banding in Fig. 3, the slow component shows no banding. In addition, the amplitude of the fast component approaches zero on the Si frame, where no TiN film is present, while the slow component maintains a nonzero amplitude.

Further investigation is needed to confirm the mechanisms that give rise to this behavior, but our current hypothesis is as follows: when a laser pulse hits the back side of the TKID, all photons that are not reflected are absorbed in the first few microns of Si. When absorbed, the photons produce athermal phonons with energies above the superconducting gap of TiN. While many of the phonons downconvert before reaching the TiN film, some are able to reach the film and directly break Cooper pairs, increasing the film's kinetic inductance beyond what purely thermal effects would cause. This effect is stronger when the laser is pointed at an area of high current density because the athermal phonons would be slightly concentrated around the laser spot, and phonons that hit the film where current density is larger would have a larger effect due to the nonlinear current dependence of kinetic inductance. The excess quasiparticles then recombine on the timescale of our fast-decay time (41 μs), returning the TKID to its expected thermal behavior after 10 s of microseconds, which in turn decays back to its quiescent state on the timescale of our slow-decay time (168 μs). This would explain why the distribution of the fast-decay amplitude follows the current density in the TKID while the slow-decay amplitude remains largely position independent: the fast decay corresponds to an early excess of athermal quasiparticles whose effect varies based on local current density, and the slow component corresponds to the device's bulk thermal behavior, which is largely unaffected by local variations in current density. We note this is not the only plausible explanation. For example, if the effective thermal conductivity in the island is lower than expected, an energy deposit could cause localized heating that peaks quickly before spreading to the rest of the island. Device response could be similarly enhanced if this heating occurred near regions of high current density. More work is needed to determine the precise mechanism.

The upper leg would see increased response for similar reasons, especially given our laser spot diameter is comparable to the width of the leg. However, the response here is further boosted by two effects: first, the TiN leads on this leg have roughly the same number of squares as the TKID island, meaning the leads have around the same kinetic inductance contained in a smaller area. Second, the leg has a much lower heat capacity than the island, meaning that energy deposited in the leg will result in a larger local temperature excursion than it would have had it been deposited in the island. These effects together could explain why both the fast-decay and slow-decay components are larger here. That said, we expect the upper leg to have a small effect on the overall energy resolution of the detector given the leg's small area compared to the island (the cross-sectional area of the island is about 60 times that of the upper leg).

Finally, we note that the measured position dependence varies more smoothly than the underlying current density, suggesting that there is some region over which the effect is averaged. The size of this region is likely linked to the scale and location of the exciting phenomenon, in this case our laser spot. We expect that an event with greater spatial extent would average over more of the current density variation, as the phonons and heat generated would cover a larger area. Similarly, an event that occurs further from the film, i.e., closer to the back side of the device, would also average over a larger area given the phonons and heat generated would have more time to spread before reaching the film. The size of the smoothing region would

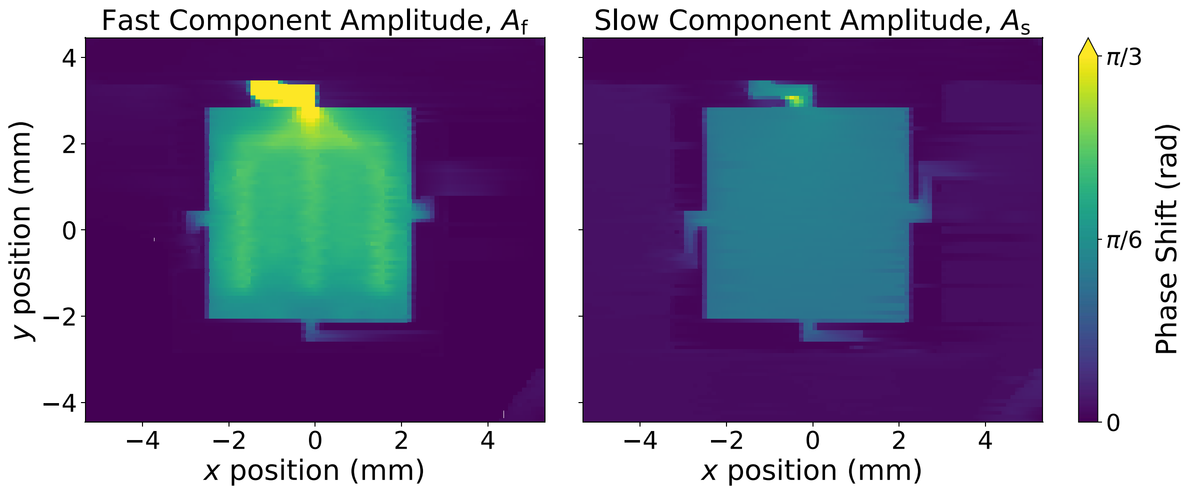

Fig. 6. Position dependence of the fast and slow TKID pulse components. The left and right panels show the amplitude of the fast and slow components, respectively, in units of resonator phase shift. Note that the color scale varies only over values from 0 to $\pi/3$. This is done to emphasize the key features of the two distributions, namely, the banding that is predominantly present in the map of the fast component. Anomalous bright areas appear in each distribution between the upper leg and the TKID island. We believe these are due to light that is absorbed in excess Si left over from the DRIE process or that is reflected off of the TKID device box lid and absorbed directly in the TiN film.

likely vary significantly for different particles and energies of interest, as each particle species could behave quite differently in the Si absorber. For example, we expect a 1 MeV gamma ray, which is quite penetrative in Si and could be absorbed close to the TiN film, to show more severe position dependence than our 1 MeV laser pulses, which are absorbed very close to the surface of the absorber.

IV. Conclusion

In this article, we have measured the position-dependent response of TKIDs designed to detect particles with MeV-scale energy and have done so using cryogenic beam steering with a MEMS mirror. The measured regions with enhanced response are in excellent agreement with calculated regions of high current density in the TKID superconducting film. In particular, the response increased in areas of high current density near the inductor sidewalls, as well as in a region of high kinetic inductance that connects the inductor on the TKID island to the interdigitated capacitor (IDC). That said, when fitting pulses to a double exponential decay, only the fast component is seen to show this position dependence. Thus, until this particular source of position dependence is mitigated, we see potential for improving TKID energy resolution in analysis by evaluating pulse size using only the slow component of the pulse.

We also believe it should be possible to design TKIDs that have minimal current-dependent positional effects. Given the way in which the variation in device response is smoothed compared to the underlying current density, we believe that the current-linked position dependence could potentially be averaged out by reducing feature sizes in the film below the spatial scale of the smoothing. For example, using narrower inductor traces could space current density variations more finely, and the smoothing effect would then result in a more consistent response across the device. A simple change like this would have other knock-on effects for the device, but we believe these effects could be mitigated with other changes in geometry. Some TKID applications could potentially also see benefits from using a thicker absorber, but this would likely only work for some particle species and energy ranges (for example, detection of minimum-ionizing particles would likely see no benefit from this since the particles would deposit energy along the absorber's entire thickness). Alternatively, this current-based behavior could be avoided entirely by separating the inductor from the absorber, although we believe this may exacerbate other position-dependent effects. We have plans to fabricate and test TKIDs with narrower inductor traces and more experimental inductor geometries to explore this theory further. We also note here that given some of the similarities between our detectors and phonon-mediated KIDs [40], [41], [42], primarily the use of large silicon absorbers and indirect Cooper pair breaking, our results may be informative for future work on those types of detectors as well.

Aside from future design and fabrication tests, there is still more work to be done exploring position dependence. First, more data are needed to test our theory about the mechanism behind the position-dependent banding in the response of our TKID. By repeating these MEMS mirror scans with varying readout powers, which should vary the current density in the film, or using photons with energy below the Si band gap, which should be absorbed primarily in the TiN film rather than the Si absorber, we could examine to a greater extent the role that current density plays. In addition, if scans were performed at multiple temperatures, potentially more information could be gleaned about the relationship between the current-dependent and thermal effects in the device. In particular, the varying heat capacity of the silicon absorber could affect the balance of these two components at different temperatures. Second, even if TKIDs can be designed to avoid the current-dependent position dependence, the other features noted in Section III are of a nonnegligible scale and must also be reduced to improve device resolution past the part in the ten scale. We believe these features are largely connected to the thermal and geometric characteristics of the device, but more testing and modeling are needed to definitively identify their sources. That said, we see significant potential for improvement with these new measurement and analysis techniques.

IV. Acknowledgment

Certain commercial equipment, instruments, or materials are identified in this article in order to specify the experimental procedure adequately. Such identification is not intended to imply recommendation or endorsement by the National Institute of Standards and Technology, nor is it intended to imply that the materials or equipment identified are necessarily the best available for the purpose.

References

[1] K. D. Irwin, G. C. Hilton, D. A. Wollman, and J. M. Martinis, "X-ray detection using a superconducting transition-edge sensor microcalorimeter with electrothermal feedback," *Appl. Phys. Lett.*, vol. 69, no. 13, pp. 1945–1947, Sep. 1996.

[2] K. D. Irwin and G. C. Hilton, "Transition-edge sensors," in *Cryogenic Particle Detection, Ser. Topics in Applied Physics*, vol. 99. C. Enss, Ed., Berlin, Germany. Springer, 2005, pp. 63–150.

[3] J. N. Ullom and D. A. Bennett, "Review of superconducting transition-edge sensors for X-ray and gamma-ray spectroscopy," *Supercond. Sci. Technol.*, vol. 28, no. 8, Aug. 2015, Art. no. 84003.

[4] W. B. Doriese et al., "A practical superconducting-microcalorimeter X-ray spectrometer for beamline and laboratory science," *Rev. Sci. Instrum.*, vol. 88, no. 5, May 2017, Art. no. 53108.

[5] S. Lee et al., "Generic character of charge and spin density waves in superconducting cuprates," *Proc. Nat. Acad. Sci.*, vol. 119, no. 15, Apr. 2022, Art. no. e2119429119.

[6] P. Szypryt et al., "A transition-edge sensor-based X-ray spectrometer for the study of highly charged ions at the National Institute of Standards and Technology electron beam ion trap," *Rev. Sci. Instrum.*, vol. 90, no. 12, Dec. 2019, Art. no. 123107.

[7] S. Okada et al., "X-ray spectroscopy of muonic atoms isolated in vacuum with transition edge sensors," *J. Low Temp. Phys.*, vol. 200, no. 5, pp. 445–451, Sep. 2020.

[8] T. Okumura et al., "Few-electron highly charged muonic Ar atoms verified by electronic K X-rays," *Phys. Rev. Lett.*, vol. 134, no. 24, Jun. 2025, Art. no. 243001.

[9] J. W. Fowler et al., "A reassessment of absolute energies of the X-ray L lines of lanthanide metals," *Metrologia*, vol. 54, no. 4, pp. 494–511, Aug. 2017.

[10] J. W. Fowler et al., "Absolute energies and emission line shapes of the L X-ray transitions of lanthanide metals," *Metrologia*, vol. 58, no. 1, Feb. 2021, Art. no. 15016.

[11] D. Barret et al., "The Athena X-ray Integral Field Unit: A consolidated design for the system requirement review of the preliminary definition phase," *Exp. Astron.*, vol. 55, no. 2, pp. 373–426, Apr. 2023.

[12] F. Shirazi et al., "511-CAM mission: A pointed 511 keV gamma-ray telescope with a focal plane detector made of stacked transition edge sensor microcalorimeter arrays," *J. Astron. Telescopes, Instruments, Syst.*, vol. 9, no. 02, May 2023, Art. no. 24006.

[13] R. C. Jaklevic, J. Lambe, A. H. Silver, and J. E. Mercereau, "Quantum interference effects in Josephson tunneling," *Phys. Rev. Lett.*, vol. 12, no. 7, pp. 159–160, Feb. 1964.

[14] J. Clarke and A. I. Braginski, *The SQUID Handbook: Fundamentals and Technology of SQUIDs and SQUID Systems*. Weinheim, DE, USA: Wiley-VCH Verlag GmbH and Co KGaA, May 2004.

[15] W. B. Doriese et al., "Developments in time-division multiplexing of X-ray transition-edge sensors," *J. Low Temp. Phys.*, vol. 184, no. 1, pp. 389–395, Jul. 2016.

[16] J. A. B. Mates et al., "Simultaneous readout of 128 X-ray and gamma-ray transition-edge microcalorimeters using microwave SQUID multiplexing," *Appl. Phys. Lett.*, vol. 111, no. 6, Aug. 2017, Art. no. 62601.

[17] J. D. Gard et al., "A scalable readout for microwave SQUID multiplexing of transition-edge sensors," *J. Low Temp. Phys.*, vol. 193, no. 3, pp. 485–497, Nov. 2018.

[18] M. Durkin et al., "Demonstration of Athena X-IFU compatible 40-Row time-division-multiplexed readout," *IEEE Trans. Appl. Supercond.*, vol. 29, no. 5, Aug. 2019, Art. no. 2101005.

[19] P. K. Day, H. G. LeDuc, B. A. Mazin, A. Vayonakis, and J. Zmuidzinas, "A broadband superconducting detector suitable for use in large arrays," *Nature*, vol. 425, no. 6960, pp. 817–821, Oct. 2003.

[20] J. Gao, "The physics of superconducting microwave resonators," Ph.D. dissertation, California Inst. Technol., Pasadena, CA, USA, Jun. 2008.

[21] J. Zmuidzinas, "Superconducting microresonators: Physics and applications," *Annu. Rev. Condens. Matter Phys.*, vol. 3, no. 1, pp. 169–214, Mar. 2012.

[22] T. Cecil et al., "Kinetic inductance detectors for X-ray spectroscopy," *Phys. Procedia*, vol. 37, pp. 697–702, 2012.

[23] A. Miceli, T. W. Cecil, L. Gades, and O. Quaranta, "Towards X-ray thermal kinetic inductance detectors," *J. Low Temp. Phys.*, vol. 176, no. 3, pp. 497–503, Aug. 2014.

[24] T. W. Cecil, L. Gades, T. Madden, D. Yan, and A. Miceli, "Optimization of thermal kinetic inductance detectors for X-ray spectroscopy," *IEEE Trans. Appl. Supercond.*, vol. 25, no. 3, Jun. 2015, Art. no. 2400805.

[25] G. Ulbricht, B. A. Mazin, P. Szypryt, A. B. Walter, C. Bockstiegel, and B. Bumble, "Highly multiplexible thermal kinetic inductance detectors for X-ray imaging spectroscopy," *Appl. Phys. Lett.*, vol. 106, no. 25, Jun. 2015, Art. no. 251103.

[26] P. Szypryt et al., "Large-format platinum silicide microwave kinetic inductance detectors for optical to near-IR astronomy," *Opt. Exp.*, vol. 25, no. 21, Oct. 2017, Art. no. 25894.

[27] J. W. Fowler et al., "Spectroscopic measurements and models of energy deposition in the substrate of quantum circuits by natural ionizing radiation," *PRX Quantum*, vol. 5, no. 4, Nov. 2024, Art. no. 40323.

[28] J. Fowler, I. F. Florang, N. Nakamura, D. Swetz, P. Szypryt, and J. Ullom, "Computed models of natural radiation backgrounds in qubits and superconducting detectors," *IEEE Trans. Appl. Supercond.*, vol. 35, no. 5, Aug. 2025, Art. no. 1700305.

[29] E. M. Scott et al., "Large-area TKIDs for charged particle detection," *J. Low Temp. Phys.*, vol. 209, no. 3, pp. 502–509, Nov. 2022.

[30] T. Rao et al., "Utilizing charged particle thermal kinetic inductance detectors for next generation neutron β-decay experiments," *IEEE Trans. Appl. Supercond.*.

[31] M. A. Lindeman, P. Khosropanah, and R. A. Hijmering, "Model of superconducting alternating current bolometers," *J. Appl. Phys.*, vol. 113, no. 7, Feb. 2013, Art. no. 74502.

[32] O. Quaranta, T. Cecil, L. Gades, and A. Miceli, "Mitigation of position dependence in X-rays absorbers for thermal kinetic inductance detectors," in *J. Physics: Conf. Ser.*, vol. 507, no. 4, May 2014, Art. no. 42033.

[33] M. De Lucia et al., "Limitations to the energy resolution of single-photon sensitive microwave kinetic inductance detectors," *AIP Adv.*, vol. 13, no. 12, Dec. 2023, Art. no. 125026. [Online]. Available: https://doi.org/10.1063/5.0168365

[34] N. R. Werthamer, "Theory of the superconducting transition temperature and energy gap function of superposed metal films," *Phys. Rev.*, vol. 132, no. 6, pp. 2440–2445, Dec. 1963.

[35] M. R. Vissers et al., "Proximity-coupled Ti/TiN multilayers for use in kinetic inductance detectors," *Appl. Phys. Lett.*, vol. 102, no. 23, Jun. 2013, Art. no. 232603.

[36] K. Stifter et al., "Cryogenic optical beam steering for superconducting device calibration," *J. Opt. Microsyst.*, vol. 5, no. 2, Jun. 2025, Art. no. 024503. [Online]. Available: https://doi.org/10.1117/1.JOM.5.2.024503

[37] J. W. Dean et al., "A laser scanning device for cryogenic beam steering at 20 Millikelvin," *IEEE Trans. Appl. Supercond.*, vol. 36, no. 6, Sep. 2026, Art. no. 2101407.

[38] P. Szypryt et al., "Kinetic inductance current sensor for visible to near-infrared wavelength transition-edge sensor readout," *Commun. Eng.*, vol. 3, no. 1, Nov. 2024, Art. no. 160.

[39] R. F. Stellingwerf, "Period determination using phase dispersion minimization," *Astrophysical J.*, vol. 224, Sep. 1978, Art. no. 953.

[40] A. Cruciani et al., "BULLKID: Monolithic array of particle absorbers sensed by kinetic inductance detectors," *Appl. Phys. Lett.*, vol. 121, no. 21, Nov. 2022, Art. no. 213504.

[41] D. J. Temples et al., "Performance of a phonon-mediated kinetic inductance detector at the NEXUS cryogenic facility," *Phys. Rev. Appl.*, vol. 22, no. 4, Oct. 2024, Art. no. 44045.

[42] L. Cardani et al., "Final results of CALDER: Kinetic inductance light detectors to search for rare events," *Eur. Phys. J. C*, vol. 81, no. 7, Jul. 2021, Art. no. 636.